ACS Energy LETTERS

Cite This: ACS Energy Lett. 2019, 4, 2585−2592

http://pubs.acs.org/journal/aelccp

LETTER

Deep Reconstruction of Nickel-Based Precatalysts for Water Oxidation Catalysis

Xiong Liu,[†] Kun Ni,[‡] Bo Wen,[†] Ruiting Guo,[†] Chaojiang Niu,[†] Jiashen Meng,[†] Qi Li,[†] Peijie Wu,[†] Yanwu Zhu,[‡] Xiaojun Wu,*[,‡] and Liqiang Mai*[,†]

[†]State Key Laboratory of Advanced Technology for Materials Synthesis and Processing, Wuhan University of Technology, Wuhan 430070, China

[‡]Hefei National Laboratory for Physical Sciences at the Microscale, School of Chemistry and Materials Sciences, CAS Key Laboratory of Materials for Energy Conversion, CAS Center for Excellence in Nanoscience, iChEM (Collaborative Innovation Center of Chemistry for Energy Materials), University of Science and Technology of China, Hefei 230026, People's Republic of China

Supporting Information

ABSTRACT: Oxygen evolution reaction (OER)-induced reconstruction on precatalysts generally results in surface-reconstructed catalysts with less active species and thus low mass activity. Herein, the deeply reconstructed (DR) catalyst is proposed and derived from a sub-10 nm precatalyst to achieve high-mass-activity catalysis. As a proof-of-concept, the DR-NiOOH with a multilevel nanosheet structure interconnected by sub-5 nm nanoparticles was obtained via a lithiation-induced deep reconstruction strategy. The robust DR-NiOOH with abundant active species enables its significantly enhanced mass activity (170 mV decrease in OER overpotential to achieve 5 mA mg^{-1}) and better durability (>10 days) than that of incompletely reconstructed Ni@NiOOH. Its strong corrosion resistance (30 wt % KOH, 72 h) and high thermal stability (52.8 °C, >40 h) were also confirmed. Theoretical analyses support that the unsaturated OH coverages on orthorhombic NiOOH endow its good OER-active property. This work highlights the merits of high-utilization DR catalysts toward potential catalytic applications under realistic conditions.

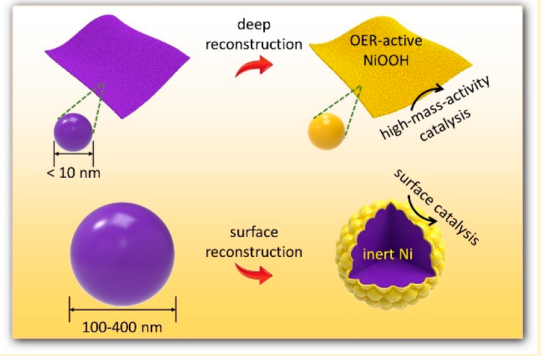

The efficiencies of energy storage/conversion devices, such as regenerative fuel cells and water electrolyzers, are primarily limited by sluggish oxygen evolution reaction (OER).[1,2] Due to its intrinsic multiple proton/electron-coupled steps and high-energy barriers,[3,4] reducing the OER overpotential remains a formidable challenge. Transition metal (TM)-based materials have recently gained substantial attention as potential IrO_2-/RuO_2-substituted catalysts, especially for Ni-based materials, due to their appropriate electronic structure for binding intermediates.[5−8] For the rational design of advanced TM catalysts, in addition to increasing the intrinsic activity of each site, exposing more active sites is crucial as well.[3] Downsizing materials to nanocatalysis units (NCUs) is an effective strategy to achieve high component utilization. To avoid aggregation and maximize catalytic performance, the integration of these NCUs to form a multilevel structured catalyst is necessary but challenging. Besides, for TM (such as Ni-,[9−11] Co-,[12] and Mn[13]-based) catalysts, electro-oxidation-induced surface reconstruction generally happens, where the real catalytic sites exist.[14,15] The reconstructed catalysts, which generally display a multicomponent core−shell structure, show inadequate utilization of inner components. The direct fabrication of catalysts with full active species is also challenging. As for Ni-based catalysts, the robust OER-active species are generally in the form of NiOOH.[16] Yet, few strategies (such as chemical oxidation,[17] sonochemical intercalation,[18] and heat treatment[19]) on its direct synthesis have been reported, and the obtained catalysts show either bulk structure or easy aggregation (Table S1), which affects the maximum exposure of active sites. Therefore, the rational design and fabrication of OER-active NCU-assembled multilevel structured catalysts is expected to realize this goal, and such a catalyst is illustrated schematically in Figure S1.

Very recently, self-reconstruction of precatalysts induced by an etching effect of the lattice anion endowed the derived catalysts with an enhanced number of active species and thus observed impressive performance.[20,21] Though the proposed strategy is limited to specific materials containing chlorine and

Received: September 2, 2019
Accepted: September 27, 2019
Published: September 27, 2019

DOI: 10.1021/acsenergylett.9b01922
ACS Energy Lett. 2019, 4, 2585−2592

Scheme 1. (a) Schematic Diagram of Size-Dependent Reconstruction Results[a] and (b) Partial Enlarged Schematic Diagram of the Ni-NiOOH Boundary, Showing the Limited Solution Penetration and Thus Low Reconstruction Degree[b]

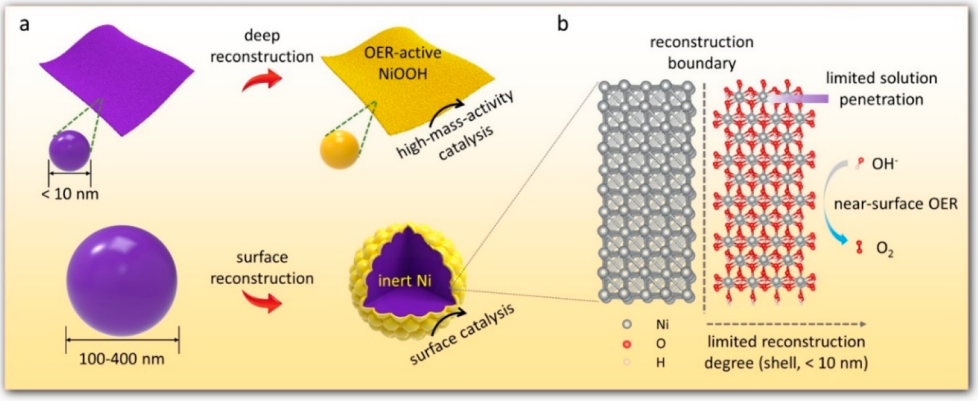

[a]The upper image displays a sub-10 nm nanoparticle-assembled Ni nanosheet and its deep reconstruction to NiOOH under OER conditions. The lower diagram shows that the surface reconstruction of the bulk Ni particle results in the core−shell Ni@NiOOH. [b]Due to the near-surface OER process, the core−shell Ni@NiOOH exhibits low-mass-activity catalysis.

fluorine, these advances inspire us to apply the deep reconstruction of bulk precatalysts as an effective strategy to achieve OER-active NCU-assembled catalysts. However, due to the reconstructed dense layer preventing electrolyte penetration for further oxidation, the deep reconstruction on bulk materials would be a great challenge. With a limited reconstruction depth of ∼10 nm,[9,11] reducing the precatalyst size to sub-10 nm greatly enlarges the contact area and results in more components being accessible to the electrolyte and thus deep/full reconstruction. As is known, lithiation-induced pulverization of the electrode degrades the battery performance.[22,23] This strategy could however be utilized to break the long-range order in bulk materials and fabricate ultrasmall grain-like precatalysts. Some reports have confirmed the lithiation-involved electrochemical tuning for advanced electrocatalysis.[24−27] Nevertheless, the lithiation strategy has not been investigated yet in reconstruction research toward fabricating NCU-assembled catalysts. As a consequence, it would be one of the promising approaches to fabricate a series of advanced deeply reconstructed (DR) catalysts with assembled NCUs to maximize utilization for various catalytic applications.

In this work, we focus on how to deepen the reconstruction degree to achieve high-mass-activity catalysis. Herein, the hierarchical DR-NiOOH sheet arrays interconnected by ultrasmall NCUs were fabricated via a lithiation-induced deep reconstruction (Li-IDR) approach. One of the prerequisites to achieve deep reconstruction is to reduce the precatalyst size (Scheme 1a). Only about a 5 nm deep surface-reconstructed NiOOH layer occurs on the bulk Ni precatalyst, and the limited reconstruction degree is attributed to the blocked electrolyte penetration (Scheme 1b). Because the lithiation process breaks material size to sub-10 nm, these ultrasmall nanoparticles could undertake deep reconstruction to NiOOH by electro-oxidation. More intriguingly, the DR catalyst shows the significantly increased number of catalytic species and the polycrystalline characteristic with abundant defects. Accordingly, the as-fabricated DR-NiOOH enables enhanced mass activity and stable catalysis for both alkaline OER and urea oxidation reaction (UOR), meanwhile displaying potential catalytic applications under realistic conditions (such as high temperature and strong alkaline solution). Besides, with the identified structure on DR-NiOOH, theoretical insights on orthorhombic NiOOH demonstrate the effects of OH coverages on its high OER activity.

In the synthesis of DR-NiOOH, the NiO sheet arrays grown on the nickel foam (NiO/NF) were first synthesized by a simple hydrothermal-calcination method (Figure S2). Next, via coin cell assembly and a galvanostatic discharging test, a one-cycle lithiation process on NiO sheets leads to their entire structure cracking and the formation of ultrasmall Ni and Li_2O nanoparticles (Figure S3a). The Li_2O can be easily removed by deionized water, which enables small interstices within the nanoparticle-assembled Ni nanosheets. Due to the oxygen-sensitive property, these Ni nanoparticles are easily oxidized to ultrasmall NiO (denoted as lithiated NiO) nanoparticles when exposed in the air. Herein, the selected substrates are recommended to be inert to lithium, which will result in the retained toughness and integrity. Besides, the nickel foam-supported NiO sheets provide good electrical contact, which is favorable for catalyst integration and the following catalysis.[6,21] Subsequently, the electro-oxidation process was carried out via 60 cycle cyclic voltammetry (CV) measurements in alkaline solution to obtain stable catalysts. When applying a voltage bias, the electro-oxidation process enables the ultrasmall NiO precatalyst to evolve to NiOOH. For comparison and to investigate the size effects on reconstruction degree, the bulk Ni particles on the nickel foam were fabricated via a H_2-reduction calcination method (Figure S3b). Through a similar electro-oxidation process, the surface-reconstructed core−shell Ni@NiOOH grown on the nickel foam (Ni@NiOOH/NF) was obtained.

The scanning electron microscopy (SEM) image confirms the well-retained sheet morphology of lithiated NiO (Figure S3c). NiO was reported to be thermodynamically unstable under electro-oxidation conditions, and stable NiOOH could be formed on its surface.[28] Nevertheless, the phase structure of NiOOH derived from NiO is unexplored. Herein, after in situ reconstruction, the lithiated NiO reconstructs to NiOOH, which displays a sheet structure assembled by the smaller nanosheets (Figures 1a and S3d). From the high-resolution transmission electron microscopy (HRTEM) image, the reconstructed NiOOH nanosheets are polycrystalline and interconnected by sub-5 nm grains with different grain

DOI: 10.1021/acsenergylett.9b01922
ACS Energy Lett. 2019, 4, 2585−2592

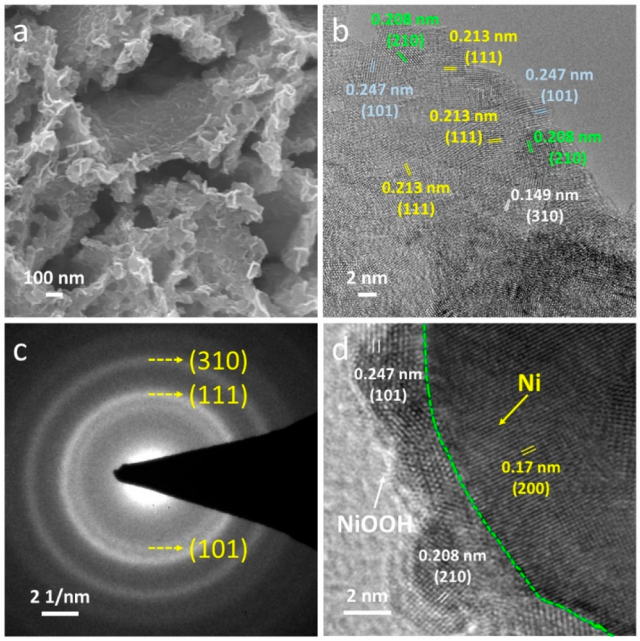

Figure 1. Characterizations on DR-NiOOH and Ni@NiOOH catalysts. (a) SEM, (b) HRTEM images, and (c) SAED pattern of DR-NiOOH. (d) HRTEM image of Ni@NiOOH.

orientations (Figure 1b). Clear lattice fringes of 0.149, 0.208, 0.213, and 0.247 nm are commonly observed and well-indexed to the (310), (210), (111), and (101) planes of orthorhombic NiOOH (JCPDS No. 27-956), respectively. No fringes can be assigned to the NiO phase, indicating complete reconstruction from NiO to NiOOH. Furthermore, the selected area electron diffraction (SAED) pattern showing a ring pattern is indicative of polycrystalline NiOOH for the reconstructed product (Figure 1c). Note that the orthorhombic NiOOH catalyst with an NCU-interconnected multilevel structure is first fabricated, which is expected to be obtained by the Li-IDR strategy of various Ni-based materials, such as phosphides, sulfides, and nitrides.

After H_2-reduction calcination, the NiO sheets evolve to bulk Ni particles due to the aggregation. The interconnected Ni particles display a smooth surface 100−400 nm in size (Figure S3e,f). After the same electro-oxidation process, the surface of Ni particles becomes rough (Figure S4a). The surface reconstruction on the Ni particles results in the core−shell structure, which was clearly demonstrated by TEM and HRTEM images (Figures 1d and S4b). An obvious interface is visible with the outer part of polycrystalline NiOOH and the inner part of monocrystalline Ni. The depth of surface reconstruction is ∼5 nm (Figure S4b,c), and the dense NiOOH layer prevents solution penetration and thus results in limited oxidative reconstruction.

Surface chemical states of DR-NiOOH and Ni@NiOOH were investigated by X-ray photoelectron spectroscopy (XPS). For NiOOH, the deconvoluted Ni $2p_{3/2}$ spectrum shows clear peaks at 856.3 and 855.3 eV, which represent the Ni^{3+}

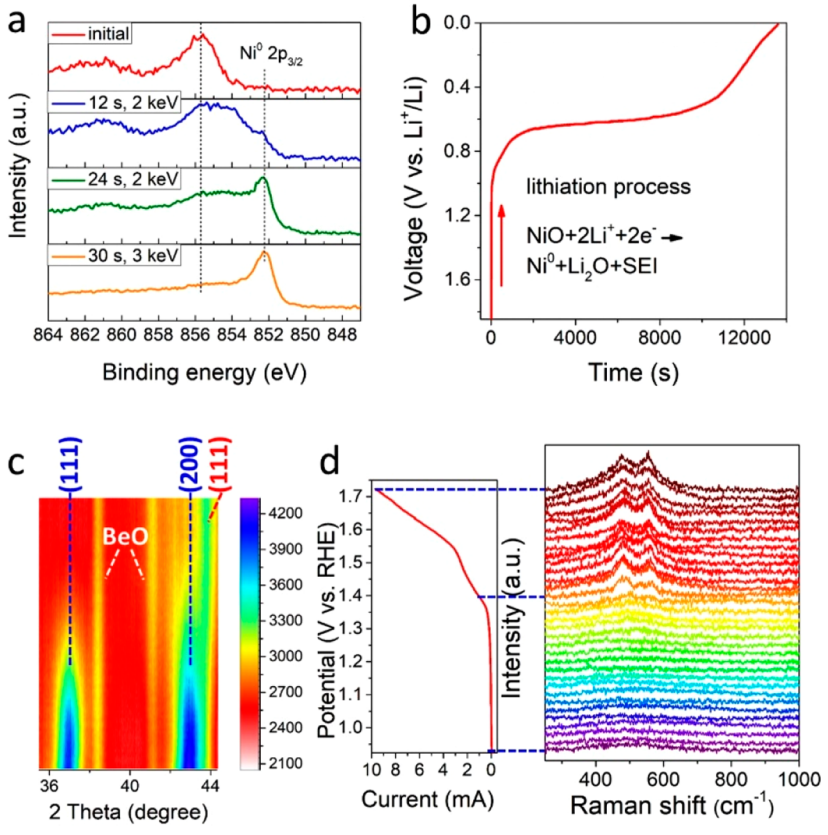

Figure 2. (a) High-resolution depth-sputtering Ni 2p XPS spectra of Ni@NiOOH/NF. (b) First galvanostatic discharging curve of the NiO anode at 300 mA g^{-1}. (c) Corresponding in situ XRD patterns showing the conversion reaction of NiO to Ni. (d) Recorded LSV curve and corresponding in situ Raman spectra with a potential interval ΔV of 25 mV (0.924−1.724 V_{RHE}), revealing the formation of NiOOH after the electro-oxidation process.

DOI: 10.1021/acsenergylett.9b01922
ACS Energy Lett. 2019, 4, 2585−2592

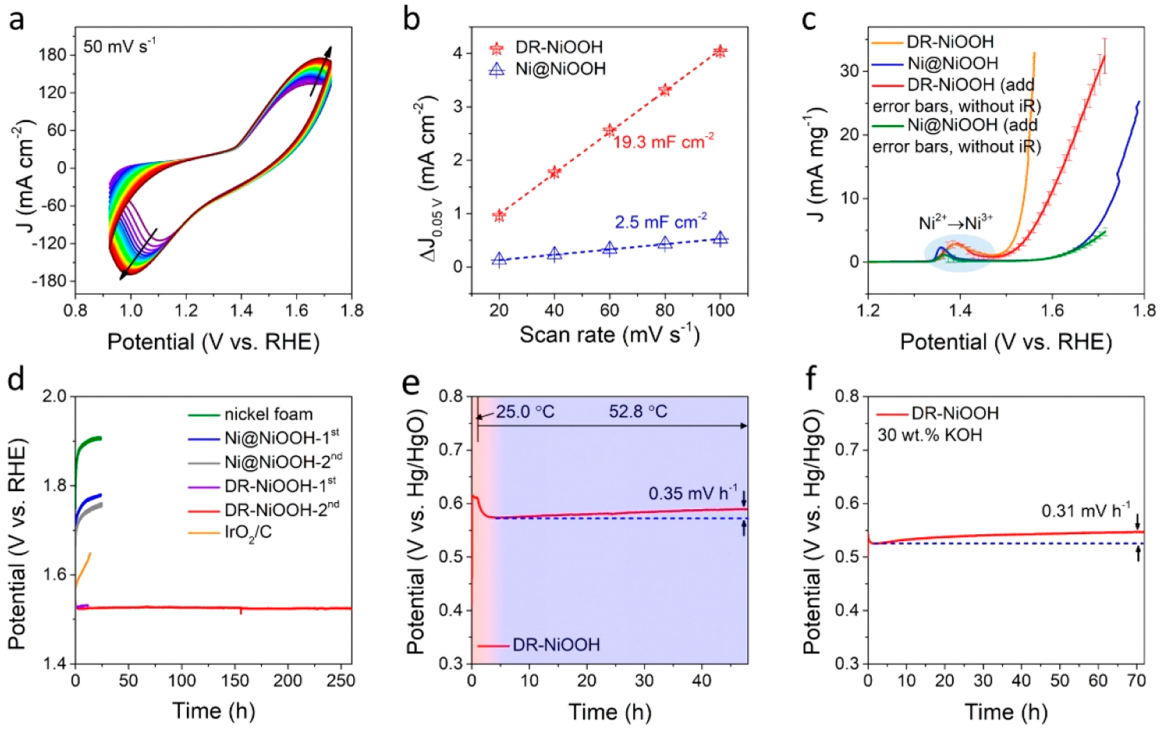

Figure 3. (a) Initial 30 cycle CV curves of lithiated NiO in 0.924−1.724 V_{RHE}. (b) Charging current density differences ($\Delta j = j_a - j_c$) as a function of the scan rate for DR-NiOOH and Ni@NiOOH. (c) Mass activity of DR-NiOOH and Ni@NiOOH with *iR* compensation. OER polarization curves of DR-NiOOH and Ni@NiOOH without *iR* compensation with error bars. (d) Chronopotentiometry measurements of catalysts measured in 1 M KOH at 10 mA cm^{-2} and at 25.0 °C. (e) Chronopotentiometry measurement of DR-NiOOH measured in 1 M KOH at 10 mA cm^{-2} and at 25.0 °C for the initial 1 h and then increasing the solution temperature to 52.8 °C. (f) Chronopotentiometry measurement of DR-NiOOH measured in 30 wt % KOH at 10 mA cm^{-2} and at 25.0 °C.

oxidation state of NiOOH and Ni^{2+} species, respectively (Figure S4d).[11,29] The Ni $2p_{3/2}$ spectrum of Ni@NiOOH is similar to that of NiOOH and displays no obvious peak shift, suggesting a negligible electronic interaction between the core and shell in Ni@NiOOH. Besides the electron microscopic characterization, the XPS Ar^+ sputtering measurement of Ni@NiOOH/NF also gives evidence that the Ni core is fully covered by NiOOH (Figure 2a). Initially, no Ni^0 $2p_{3/2}$ XPS peak could be observed. After sputtering the surface with Ar^+ for 12 and 24 s, the intensity of the Ni^0 $2p_{3/2}$ peak gradually increases. The Ni $2p_{3/2}$ peak at 854−857 eV almost disappears after sputtering for 30 s, thereby clearly demonstrating its core−shell structure.

To uncover the Li-IDR mechanism, in situ X-ray diffraction (XRD) measurements were first carried out to monitor the first-cycle lithiation process of NiO powder. The first-discharging curve depicts an obvious platform at ∼0.6 V vs Li^+/Li where the conversion reaction happens (Figure 2b). A previous report demonstrated that the Ni^0 and Li_2O served as the main discharging products.[30] The formation of Ni^0 was revealed (Figure 2c). Before lithiation, the sharp peaks at 37.3 and 43.3° from XRD patterns pertain to the (111) and (200) planes of cubic NiO (JCPDS No. 04-0835). After discharging, the NiO peaks gradually become weak and disappear, indicating breaking of the Ni−O bonds and complete crack of the NiO structure after Li intercalation. Meanwhile, a new peak at ∼44° emerges, which is indexed to the (111) plane of cubic Ni (JCPDS No. 89-7128). After fully discharging to 0.01 V, the products are washed by plenty of ethanol and water to remove Li_2O and residual electrolyte. When exposed to air, these ultrasmall Ni nanoparticles are gradually oxidized to nanosized NiO (Figure S5). The formed NiO nanoparticles could be interconnected, which may be due to half of a cycle of the lithiation process.

To further recognize the OER-active species, the in situ electrochemical-coupled Raman (EC-Raman) measurements were operated to achieve real-time detection (Figure 2d). The lithiated NiO@NF directly served as the working electrode, and the graphite rod and unused Hg/HgO electrode served as the counter electrode and reference electrode, respectively. The Raman data were synchronously recorded when the catalytic test was conducted. From the linear sweep voltammetry (LSV) curve, the onset potential was about 1.40 V vs RHE (denoted as V_{RHE}). When the applied voltage bias is higher, the two Raman peaks at 474 and 554 cm^{-1} emerge, which refer to the e_g bending and A_{1g} stretching vibration of Ni−O in NiOOH,[31] respectively. The Raman peaks of DR-NiOOH remain under further oxidation, which suggests it as a robust OER-active species.

OER performance was evaluated in a standard three-electrode system. To achieve a stable catalyst and intrinsic OER activity, the reconstruction, which was so-called "activation", was conducted by CV measurements (Figure 3a). The current densities of the reduction peak at ∼1.0 V_{RHE} and the oxidation peak at ∼1.6 V_{RHE} increase gradually during 1−20 CV cycles and remain basically unchanged during 25−30 CV cycles (Figure S6). Therefore, the stable current densities of redox peaks indicate that the reconstruction is almost accomplished after 30 cycle CV measurements. After reconstruction, the LSV curves of nickel foam, Ni@NiOOH derived from bulk Ni particles, DR-NiOOH derived from lithiated NiO, and the commercial IrO_2/C were measured at a

DOI: 10.1021/acsenergylett.9b01922
ACS Energy Lett. 2019, 4, 2585−2592

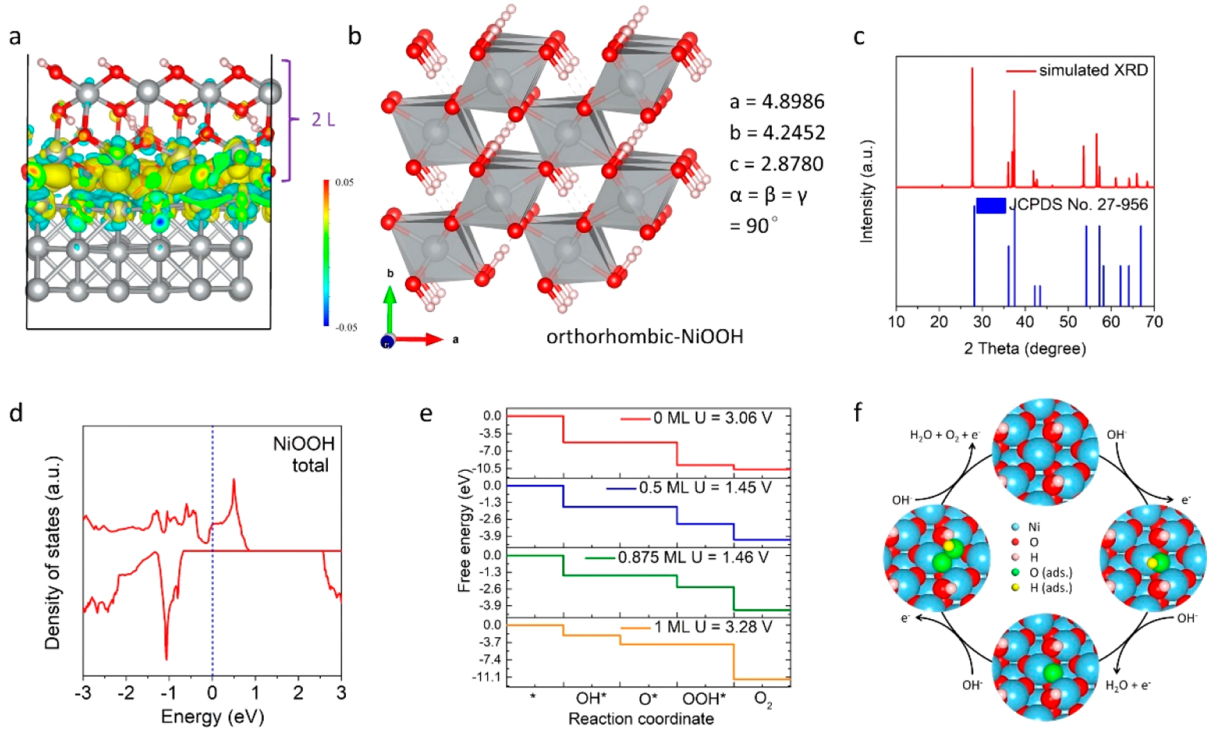

Figure 4. (a) Calculated differential charge density of the Ni-2 L NiOOH model. The value for the isosurface is 0.005 e Bohr^{-3}. The thickness of 1 L NiOOH is ~0.25 nm. (b) Crystal structure and parameters of orthorhombic-NiOOH. (c) Simulated XRD pattern based on the optimized NiOOH model and well-matched with the standard card. (d) Calculated DOS for NiOOH. The Fermi level was set at 0 eV. (e) Free energy diagram for the four elementary steps on NiOOH(101) with different OH coverages of 0, 0.5, 0.875, and 1 ML at the potential to start reaction. (f) OER mechanism on NiOOH with the optimal structure of 0.5 ML at each stage.

low scan rate of 1 mV s^{-1} (Figure S7a). The bare nickel foam exhibits negligible OER activity, which eliminates the effect of the substrate for the loading catalysts as much as possible. To generate a current density of 10 mA cm^{-2}, the NiOOH requires a low overpotential (η_{10}) of 281−296 mV, which exhibits comparable performance to some recently reported Ni-based OER catalysts (Table S2). However, the η_{10} of Ni@NiOOH is as high as 439 mV. The large overpotential decrease of DR-NiOOH demonstrates its significantly enhanced OER activity. To display the advantage of the DR catalyst, the electrochemically active surface area (ECSA) and LSV curves normalized by mass of the supported NiOOH are compared. The ECSA of DR-NiOOH and Ni@NiOOH was evaluated by measuring double-layer capacitance (C_{dl}), which is typically used to represent ECSA.[20] The C_{dl} of DR-NiOOH is 7.72 times that of Ni@NiOOH (2.5 mF cm^{-2}), indicating that the DR-NiOOH possesses higher ECSA and thus more exposure of active sites (Figures 3b and S9). Besides, the DR-NiOOH with more OER-active species can access more electrolyte than the core−shell Ni@NiOOH catalyst, and the latter possesses an inactive core. Therefore, the obviously higher mass activity is achieved for DR-NiOOH than that of Ni@NiOOH when analyzing the LSV curves normalized by mass (Figure 3c).

The catalytic stability of all samples was also examined via the chronopotentiometry technique (Figure 3d). The DR-NiOOH exhibits the best OER stability with durability for 260 h, which is much better than other samples. Importantly, the nanosheet-assembled sheet morphology for DR-NiOOH remains after a 1 day continuous chronopotentiometry test (Figure S10a). The stable porous structure is conducive to gas emission in the OER process, which is one reason for the stable performance of DR-NiOOH. From the HRTEM image, the lattice fringes of 0.149, 0.208, 0.213, and 0.247 nm can be indexed to the (310), (210), (111), and (101) planes of orthorhombic NiOOH, further demonstrating that it is a robust OER catalyst with good phase stability (Figure S10b). To satisfy the potential commercial water−alkali electrolyzer applications, two parameters, strong corrosion resistance (evaluated at 30 wt % KOH solution[32]) and high thermal stability (cell temperature at 50−80 °C[33]) of the catalysts, are also required. As shown in Figure 3e, using a new Hg/HgO electrode, the DR-NiOOH remains with an OER potential of 0.61 $V_{Hg/HgO}$ at 25.0 °C for the initial 1 h. Then, increasing the solution temperature to 52.8 °C, DR-NiOOH can retain its OER catalysis for >40 h with a performance decay rate of only 0.35 mV h^{-1}. While using 30 wt % KOH as an electrolyte, the DR-NiOOH can deliver stable and continuous OER catalysis at 25.0 °C for 72 h (Figure 3f). Overall, we first demonstrate the obtained DR-NiOOH with strong corrosion resistance and high thermal stability during OER measurements, and our results also highlight the potential of DR-NiOOH in practical applications.

As discussed above, DR-NiOOH shows superior OER performance than the surface-reconstructed Ni@NiOOH. The reasons for the higher OER performance of DR-NiOOH are analyzed as follows. (1) The DR catalyst shows more OER-active NiOOH and catalytic sites, but the inner core in the incompletely reconstructed one is undeveloped and inactive. Generally, two-component contact can affect the electronic properties within the first few nanometers from contact.[34] In addition, the density functional theory (DFT) calculations on alloy−carbon models revealed that the effects of metal clusters on the carbon shell would decline while the shell was more than three layers.[35] Therefore, for Ni@NiOOH catalysts with

DOI: 10.1021/acsenergylett.9b01922
ACS Energy Lett. 2019, 4, 2585−2592

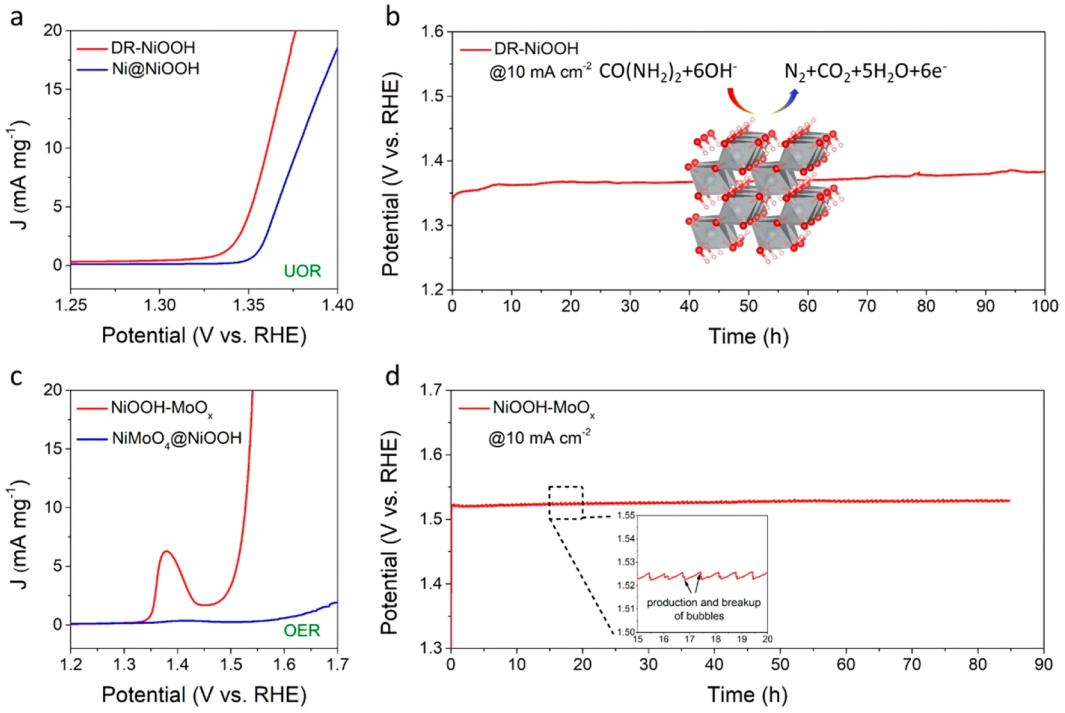

Figure 5. (a) UOR polarization curves of DR-NiOOH and Ni@NiOOH normalized by mass. (b) Chronopotentiometry measurement of DR-NiOOH. (c) Mass activity of NiOOH-MoO$_x$ and NiMoO$_4$@NiOOH. (d) Chronopotentiometry measurement of NiOOH-MoO$_x$.

the thickness of the dense shell larger than several nanometers, the electronic effect between the core and shell might be negligible. Here, models of Ni(200) clusters with two- to five-layer NiOOH(101) covered on the Ni surface (denoted as Ni-x L NiOOH, x represents a value of 2−5) were established according to the experimental results (Figures S12 and S13a−d). The differential charge densities based on the above four models were calculated (Figures 4a and S13e−g), showing that the charge transfer is highly localized at interfaces, with the O atoms serving as electron acceptors and Ni atoms serving as electron donors. Even for the Ni-2 L NiOOH model, the electron concentration of the outer layer exposed to vacuum is almost unchanged. Considering that the thickness of 2 L NiOOH (~0.50 nm) is much smaller than the experimental value (at least 2 nm), the enclosed Ni core should have a negligible effect on the catalytic procedure of the NiOOH surface. Therefore, the core−shell Ni@NiOOH catalyst shows low utilization due to the inactive Ni core. (2) The intensity of the oxidation peak ($Ni^{2+} \rightarrow Ni^{3+}$, ~1.38 V_{RHE}) for DR-NiOOH is higher (Figure 3c), which indicates abundant active species. In addition, the nanoparticle-interconnected nanosheet structure of DR-NiOOH allows better contact, which endows the continuous electron transport.[36] Therefore, the DR-NiOOH shows a much lower charge transfer resistance (R_{ct}) of 24 Ω than that of Ni@NiOOH (425 Ω, Figure S14), which contributes to excellent OER activity of DR-NiOOH. (3) The DR-NiOOH displays an ultrasmall nanosheet-assembled sheet-like morphology, which guarantees stable catalysis, more catalytic sites, and easy electrolyte penetration. (4) The polycrystalline/low-crystalline DR-NiOOH indicates abundant defects, which have also been reported to improve OER activity.[20] Therefore, the DR catalysts show great potential as high-efficiency OER catalysts.

The component and OER-active species of DR-NiOOH are identifiable with the orthorhombic-phase NiOOH. Herein, the OER catalytic mechanism of orthorhombic-phase NiOOH was studied by DFT calculations. Isotypic with InOOH,[37,38] the simulated NiOOH structure is shown in Figure 4b with the space group of $P21nm$ (space group 31; a = 4.8986 Å, b = 4.2452 Å, c = 2.8780 Å, $\alpha = \beta = \gamma = 90°$). The simulated XRD pattern based on its structure is highly consistent with the standard PDF card (JCPDS No. 27-956, Figure 4c and Table S3), which indicates the accuracy of the obtained NiOOH crystal structure. The density of states (DOS) of NiOOH at the Fermi level shows a continuous peak (Figure 4d), which reveals its intrinsic half-metallic character. Combined with the low R_{ct} value in the OER experiment, the NiOOH is supposed to provide faster electron transfer during OER. To uncover the OER process of NiOOH, the (101) plane was rationally selected for further calculations because it requires a relatively small simulation cell among the experimental observed planes. The free energy (ΔG) diagrams with different OH coverages (θ_{OH*}) of 0, 0.5, 0.875, and 1 ML in alkaline solution on the Ni-terminated (101) planes were analyzed (Figures 4e, S15, and 16). Generally, the OER activity is determined by the descriptor of the free energy difference ($\Delta G_{O*} - \Delta G_{OH*}$).[39] For the models with θ_{OH*} of 0.5 and 0.875 ML, the calculated applied potentials to make reaction happen are 1.45 and 1.46 V, respectively, which means that the required overpotentials for them are 1.04 and 1.05 V. These overpotential values are consistent with the previously reported value for β-NiOOH.[40] However, the required applied potentials are much larger on the 0 ML (3.06 V) and 1 ML (3.28 V) models. Therefore, the NiOOH with the unsaturated OH coverages possesses high OER activity. Unlike NiOOH with OH coverages of 0, 0.5, and 0.875 ML, the rate-determining step for the 1 ML model is determined by the descriptor of $\Delta G_{OOH*} - \Delta G_{O*}$, which is attributed to the weak adsorption of the OOH group on the 1 ML surface. Accordingly, we give the optimized pathways of alkaline OER on the NiOOH with a θ_{OH*} of 0.5 ML (Figures

DOI: 10.1021/acsenergylett.9b01922
ACS Energy Lett. 2019, 4, 2585−2592

4f and S17) and other θ_{OH*} values (Figures S18−20). The schematic OER process on NiOOH proceeds through the four elementary steps, consisting of three intermediates, i.e., OH*, O*, and OOH*.[3,41] According to our simulation, the OER steps happen on the NiOOH surface at the OH vacant sites, and this conclusion is in accordance with the reported β-NiOOH.[42]

To further confirm the advantages of the DR catalyst, the UOR activity was evaluated in 1 M KOH with 0.5 M urea. Similar to the OER, the UOR ($CO(NH_2)_2 + 6OH^- \rightarrow N_2 + CO_2 + 5H_2O + 6e^-$) undergoes sluggish kinetics as well and requires highly effective catalysts to accelerate the catalytic kinetics. For nickel-based materials, the newly generated NiOOH has been confirmed as the active species for UOR.[43] Therefore, the DR-NiOOH with more active species shows higher UOR activity than that of Ni@NiOOH (Figure 5a). Besides, the excellent stability of DR-NiOOH for UOR was demonstrated, which can sustain ∼1.37 V_{RHE} for 100 h of continuous operation (Figure 5b). In addition, to confirm the effectiveness of our Li-IDR strategy, the DR-Ni-Mo-O (denoted as NiOOH-MoO_x) was also fabricated according to the aforementioned procedures (Figures S21 and S22). Due to the more OER-active NiOOH, the NiOOH-MoO_x catalyst outperforms the core−shell $NiMoO_4$@NiOOH for alkaline OER in terms of mass activity (Figure 5c). This catalyst also exhibits good stability with little potential change after continuous operation for 84 h (Figure 5d). These promotions demonstrate that the Li-IDR strategy is expected to be applied on other TM-based materials for enhanced catalytic activity for alkaline OER and UOR.

In summary, we demonstrated a Li-IDR strategy to fabricate a series of DR catalysts interconnected by NCUs, such as DR-NiOOH and NiOOH-MoO_x. The Li-IDR mechanism was uncovered by multiple techniques, including in situ XRD/Raman and ex situ TEM. Notably, deep reconstruction was achieved via downsizing of the precatalysts to sub-10 nm. The obtained DR catalysts possessed the hierarchical structure with plentiful electrolyte-accessible NiOOH, low-crystalline characteristic with abundant defects, and recognizable components. Such a unique structure enabled superior mass activity and outstanding catalytic stability for alkaline OER and UOR, even under strong corrosion or high-temperature conditions. Besides, we theoretically demonstrated that the electronic effects of inner Ni on the NiOOH shell could be negligible while the shell thickness was more than 0.5 nm. The DR catalysts with abundant active species thus possessed significant advantages over the surface-reconstructed one. In addition, the theoretical investigations revealed that the orthorhombic NiOOH with unsaturated OH coverages possessed high OER activity. The exploration of deep reconstruction, a reconstruction/OER catalytic mechanism, and electrocatalysis under more realistic conditions in this work is expected to inspire the rational design of DR catalysts interconnected by NCUs.

■ ASSOCIATED CONTENT

Supporting Information

The Supporting Information is available free of charge on the ACS Publications website at DOI: 10.1021/acsenergylett.9b01922.

Experimental section, electrochemical measurements, and calculation method; morphological and structural characterizations; calculation models and free energy diagrams; and table summaries for synthetic methods, activity comparison, cif parameters, and additional data analysis (PDF)

■ AUTHOR INFORMATION

Corresponding Authors

*E-mail: mlq518@whut.edu.cn.
*E-mail: xjwu@ustc.edu.cn.

ORCID

Yanwu Zhu: 0000-0002-7505-1502
Xiaojun Wu: 0000-0003-3606-1211
Liqiang Mai: 0000-0003-4259-7725

Author Contributions

X.L. and K.N. contributed equally to this work.

Notes

The authors declare no competing financial interest.

■ ACKNOWLEDGMENTS

This work was supported by the National Natural Science Fund for Distinguished Young Scholars (51425204), the National Key Research and Development Program of China (2016YFA0202603, 2018YFA0208603), the National Natural Science Foundation of China (51521001, 21890751, 51772282), the Fundamental Research Funds for the Central Universities (2019-zy-047), the Anhui Initiative in Quantum Information Technology, CAS Interdisciplinary Innovation Team, and the Fundamental Research Funds for the Central Universities. The numerical calculations in this paper were done on the supercomputing system in the Supercomputing Center of the University of Science and Technology of China.

■ REFERENCES

(1) Huang, Z.-F.; Song, J. J.; Du, Y. H.; Xi, S. B.; Dou, S.; Nsanzimana, J. M. V.; Wang, C.; Xu, Z. C. J.; Wang, X. Chemical and Structural Origin of Lattice Oxygen Oxidation in Co-Zn Oxyhydroxide Oxygen Evolution Electrocatalysts. *Nat. Energy* **2019**, *4*, 329−338.

(2) Park, S.; Shao, Y. Y.; Liu, J.; Wang, Y. Oxygen Electrocatalysts for Water Electrolyzers and Reversible Fuel Cells: Status and Perspective. *Energy Environ. Sci.* **2012**, *5*, 9331−9344.

(3) Seh, Z. W.; Kibsgaard, J.; Dickens, C. F.; Chorkendorff, I. B.; Nørskov, J. K.; Jaramillo, T. F. Combining Theory and Experiment in Electrocatalysis: Insights into Materials Design. *Science* **2017**, *355*, No. eaad4998.

(4) Hunter, B. M.; Gray, H. B.; Müller, A. M. Earth-Abundant Heterogeneous Water Oxidation Catalysts. *Chem. Rev.* **2016**, *116*, 14120−14136.

(5) Vij, V.; Sultan, S.; Harzandi, A. M.; Meena, A.; Tiwari, J. N.; Lee, W.-G.; Yoon, T.; Kim, K. S. Nickel-Based Electrocatalysts for Energy-Related Applications: Oxygen Reduction, Oxygen Evolution, and Hydrogen Evolution Reactions. *ACS Catal.* **2017**, *7*, 7196−7225.

(6) Asnavandi, M.; Yin, Y. C.; Li, Y. B.; Sun, C. H.; Zhao, C. Promoting Oxygen Evolution Reactions through Introduction of Oxygen Vacancies to Benchmark NiFe-OOH Catalysts. *ACS Energy Lett.* **2018**, *3*, 1515−1520.

(7) Niu, S.; Jiang, W.-J.; Wei, Z. X.; Tang, T.; Ma, J. M.; Hu, J.-S.; Wan, L.-J. Se-Doping Activates FeOOH for Cost-Effective and Efficient Electrochemical Water Oxidation. *J. Am. Chem. Soc.* **2019**, *141*, 7005−7013.

(8) He, Q.; Wan, Y. Y.; Jiang, H. L.; Pan, Z. W.; Wu, C. Q.; Wang, M.; Wu, X. J.; Ye, B. J.; Ajayan, P. M.; Song, L. Nickel Vacancies Boost Reconstruction in Nickel Hydroxide Electrocatalyst. *ACS Energy Lett.* **2018**, *3*, 1373−1380.

DOI: 10.1021/acsenergylett.9b01922
ACS Energy Lett. 2019, 4, 2585−2592

(9) Stern, L.-A.; Feng, L. G.; Song, F.; Hu, X. L. Ni_2P as a Janus Catalyst for Water Splitting: the Oxygen Evolution Activity of Ni_2P Nanoparticles. *Energy Environ. Sci.* **2015**, *8*, 2347−2351.
(10) Li, Y. B.; Zhao, C. Iron-Doped Nickel Phosphate as Synergistic Electrocatalyst for Water Oxidation. *Chem. Mater.* **2016**, *28*, 5659−5666.
(11) Sun, H. M.; Xu, X. B.; Yan, Z. H.; Chen, X.; Cheng, F. Y.; Weiss, P. S.; Chen, J. Porous Multishelled Ni_2P Hollow Microspheres as an Active Electrocatalyst for Hydrogen and Oxygen Evolution. *Chem. Mater.* **2017**, *29*, 8539−8547.
(12) Chen, P. Z.; Xu, K.; Fang, Z. W.; Tong, Y.; Wu, J. C.; Lu, X. L.; Peng, X.; Ding, H.; Wu, C. Z.; Xie, Y. Metallic Co_4N Porous Nanowire Arrays Activated by Surface Oxidation as Electrocatalysts for the Oxygen Evolution Reaction. *Angew. Chem., Int. Ed.* **2015**, *54*, 14710−14714.
(13) Walter, C.; Menezes, P. W.; Orthmann, S.; Schuch, J.; Connor, P.; Kaiser, B.; Lerch, M.; Driess, M. A Molecular Approach to Manganese Nitride Acting as a High Performance Electrocatalyst in the Oxygen Evolution Reaction. *Angew. Chem., Int. Ed.* **2018**, *57*, 698−702.
(14) Jin, S. Are Metal Chalcogenides, Nitrides, and Phosphides Oxygen Evolution Catalysts or Bifunctional Catalysts? *ACS Energy Lett.* **2017**, *2*, 1937−1938.
(15) Wygant, B. R.; Kawashima, K.; Mullins, C. B. Catalyst or Precatalyst? The Effect of Oxidation on Transition Metal Carbide, Pnictide, and Chalcogenide Oxygen Evolution Catalysts. *ACS Energy Lett.* **2018**, *3*, 2956−2966.
(16) Klaus, S.; Cai, Y.; Louie, M. W.; Trotochaud, L.; Bell, A. T. Effects of Fe Electrolyte Impurities on $Ni(OH)_2$/NiOOH Structure and Oxygen Evolution Activity. *J. Phys. Chem. C* **2015**, *119*, 7243−7254.
(17) Pan, J. Q.; Sun, Y. Z.; Wan, P. Y.; Wang, Z. H.; Liu, X. G. Synthesis, Characterization and Electrochemical Performance of Battery Grade NiOOH. *Electrochem. Commun.* **2005**, *7*, 857−862.
(18) Liu, L. P.; Zhou, Z. T.; Peng, C. H. Sonochemical Intercalation Synthesis of Nano γ-nickel Oxyhydroxide: Structure and Electrochemical Properties. *Electrochim. Acta* **2008**, *54*, 434−441.
(19) Zhang, Q.; Zhang, C. C.; Liang, L. B.; Yin, P. G.; Tian, Y. Orthorhombic α-NiOOH Nanosheet Arrays: Phase Conversion and Efficient Bifunctional Electrocatalysts for Full Water Splitting. *ACS Sustainable Chem. Eng.* **2017**, *5*, 3808−3818.
(20) Jiang, H. L.; He, Q.; Li, X. Y.; Su, X. Z.; Zhang, Y. K.; Chen, S. M.; Zhang, S.; Zhang, G. Z.; Jiang, J.; Luo, Y.; Ajayan, P. M.; Song, L. Tracking Structural Self-Reconstruction and Identifying True Active Sites toward Cobalt Oxychloride Precatalyst of Oxygen Evolution Reaction. *Adv. Mater.* **2019**, *31*, 1805127.
(21) Zhang, B. W.; Jiang, K.; Wang, H. T.; Hu, S. Fluoride-Induced Dynamic Surface Self-Reconstruction Produces Unexpectedly Efficient Oxygen-Evolution Catalyst. *Nano Lett.* **2019**, *19*, 530−537.
(22) Wu, H.; Chan, G.; Choi, J. W.; Ryu, I.; Yao, Y.; McDowell, M. T.; Lee, S. W.; Jackson, A.; Yang, Y.; Hu, L. B.; Cui, Y. Stable Cycling of Double-Walled Silicon Nanotube Battery Anodes through Solid-Electrolyte Interphase Control. *Nat. Nanotechnol.* **2012**, *7*, 310−315.
(23) Mai, L. Q.; Yan, M. Y.; Zhao, Y. L. Track Batteries Degrading in Real Time. *Nature* **2017**, *546*, 469−470.
(24) Wang, H. T.; Xu, S. C.; Tsai, C.; Li, Y. Z.; Liu, C.; Zhao, J.; Liu, Y. Y.; Yuan, H. Y.; Abild-Pedersen, F.; Prinz, F. B.; Nørskov, J. K.; Cui, Y. Direct and Continuous Strain Control of Catalysts with Tunable Battery Electrode Materials. *Science* **2016**, *354*, 1031−1036.
(25) Gao, J. J.; Xu, C.-Q.; Hung, S.-F.; Liu, W.; Cai, W. Z.; Zeng, Z. P.; Jia, C. M.; Chen, H. M.; Xiao, H.; Li, J.; Huang, Y. Q.; Liu, B. Breaking Long-Range Order in Iridium Oxide by Alkali Ion for Efficient Water Oxidation. *J. Am. Chem. Soc.* **2019**, *141*, 3014−3023.
(26) Chen, W.; Wang, H. T.; Li, Y. Z.; Liu, Y. Y.; Sun, J.; Lee, S. H.; Lee, J.-S.; Cui, Y. In Situ Electrochemical Oxidation Tuning of Transition Metal Disulfides to Oxides for Enhanced Water Oxidation. *ACS Cent. Sci.* **2015**, *1*, 244−251.
(27) Wang, H. T.; Lee, H.-W.; Deng, Y.; Lu, Z. Y.; Hsu, P.-C.; Liu, Y. Y.; Lin, D. C.; Cui, Y. Bifunctional Non-Noble Metal Oxide Nanoparticle Electrocatalysts through Lithium-Induced Conversion for Overall Water Splitting. *Nat. Commun.* **2015**, *6*, 7261.
(28) Ueta, H.; Abe, Y.; Kato, K.; Kawamura, M.; Sasaki, K.; Itoh, H. Ni Oxyhydroxide Thin Films Prepared by Reactive Sputtering Using O_2 + H_2O Mixed Gas. *Jpn. J. Appl. Phys.* **2009**, *48*, 015501.
(29) Yan, Z. H.; Sun, H. M.; Chen, X.; Liu, H. H.; Zhao, Y. R.; Li, H. X.; Xie, W.; Cheng, F. Y.; Chen, J. Anion Insertion Enhanced Electrodeposition of Robust Metal Hydroxide/Oxide Electrodes for Oxygen Evolution. *Nat. Commun.* **2018**, *9*, 2373.
(30) Varghese, B.; Reddy, M. V.; Yanwu, Z.; Lit, C. S.; Hoong, T. C.; Rao, G. V. S.; Chowdari, B. V. R.; Wee, A. T. S.; Lim, C. T.; Sow, C.-H. Fabrication of NiO Nanowall Electrodes for High Performance Lithium Ion Battery. *Chem. Mater.* **2008**, *20*, 3360−3367.
(31) Zhu, K. Y.; Zhu, X. F.; Yang, W. S. Application of In Situ Techniques for the Characterization of NiFe based Oxygen Evolution Reaction (OER) Electrocatalysts. *Angew. Chem., Int. Ed.* **2019**, *58*, 1252−1265.
(32) Guo, F. F.; Wu, Y. Y.; Chen, H.; Liu, Y. P.; Yang, L.; Ai, X.; Zou, X. X. High-Performance Oxygen Evolution Electrocatalysis by Boronized Metal Sheets with Self-Functionalized Surfaces. *Energy Environ. Sci.* **2019**, *12*, 684−692.
(33) Stamenkovic, V. R.; Strmcnik, D.; Lopes, P. P.; Markovic, N. M. Energy and Fuels from Electrochemical Interfaces. *Nat. Mater.* **2017**, *16*, 57−69.
(34) Greiner, M. T.; Chai, L.; Helander, M. G.; Tang, W.-M.; Lu, Z.-H. Metal/Metal-Oxide Interfaces: How Metal Contacts Affect the Work Function and Band Structure of MoO_3. *Adv. Funct. Mater.* **2013**, *23*, 215−226.
(35) Deng, J.; Ren, P. J.; Deng, D. H.; Bao, X. H. Enhanced Electron Penetration through an Ultrathin Graphene Layer for Highly Efficient Catalysis of the Hydrogen Evolution Reaction. *Angew. Chem., Int. Ed.* **2015**, *54*, 2100−2104.
(36) Fabbri, E.; Nachtegaal, M.; Binninger, T.; Cheng, X.; Kim, B.-J.; Durst, J.; Bozza, F.; Graule, T.; Schäublin, R.; Wiles, L.; Pertoso, M.; Danilovic, N.; Ayers, K. E.; Schmidt, T. J. Dynamic Surface Self-Reconstruction is the Key of Highly Active Perovskite Nano-Electrocatalysts for Water Splitting. *Nat. Mater.* **2017**, *16*, 925−931.
(37) Chenavas, J.; Joubert, J. C.; Capponi, J. J.; Marezio, M. Synthese de Nouvelles Phases Denses d'oxyhydroxydes $M^{3+}OOH$ des Metaux de la Premiere Serie de Transition, en Milieu Hydrothermal à Tres Haute Pression. *J. Solid State Chem.* **1973**, *6*, 1−15.
(38) Lehmann, M. S.; Larsen, F. K.; Poulsen, F. R.; Christensen, A. N.; Rasmussen, S. E. Neutron and X-ray Crystallographic Studies on Indium Oxide Hydroxide. *Acta Chem. Scand.* **1970**, *24*, 1662−1670.
(39) Zhang, B.; Zheng, X.; Voznyy, O.; Comin, R.; Bajdich, M.; Garcia-Melchor, M.; Han, L.; Xu, J.; Liu, M.; Zheng, L.; Garcia de Arquer, F. P.; Dinh, C. T.; Fan, F.; Yuan, M.; Yassitepe, E.; Chen, N.; Regier, T.; Liu, P.; Li, Y.; De Luna, P.; Janmohamed, A.; Xin, H. L.; Yang, H.; Vojvodic, A.; Sargent, E. H. Homogeneously Dispersed Multimetal Oxygen-Evolving Catalysts. *Science* **2016**, *352*, 333−337.
(40) Jiang, J.; Sun, F. F.; Zhou, S.; Hu, W.; Zhang, H.; Dong, J. C.; Jiang, Z.; Zhao, J. J.; Li, J. F.; Yan, W. S.; Wang, M. Atomic-Level Insight into Super-Efficient Electrocatalytic Oxygen Evolution on Iron and Vanadium Co-doped Nickel (Oxy)hydroxide. *Nat. Commun.* **2018**, *9*, 2885.
(41) Jiao, Y.; Zheng, Y.; Jaroniec, M.; Qiao, S. Z. Design of Electrocatalysts for Oxygen- and Hydrogen-Involving Energy Conversion Reactions. *Chem. Soc. Rev.* **2015**, *44*, 2060−2086.
(42) Tkalych, A. J.; Zhuang, H. L.; Carter, E. A. A Density Functional + U Assessment of Oxygen Evolution Reaction Mechanisms on β-NiOOH. *ACS Catal.* **2017**, *7*, 5329−5339.
(43) Zhu, X. J.; Dou, X. Y.; Dai, J.; An, X. D.; Guo, Y. Q.; Zhang, L. D.; Tao, S.; Zhao, J. Y.; Chu, W. S.; Zeng, X. C.; Wu, C. Z.; Xie, Y. Metallic Nickel Hydroxide Nanosheets Give Superior Electrocatalytic Oxidation of Urea for Fuel Cells. *Angew. Chem., Int. Ed.* **2016**, *55*, 12465−12469.

DOI: 10.1021/acsenergylett.9b01922
ACS Energy Lett. 2019, 4, 2585−2592